Preparation and Hydrogen Evolution Property Tunning of Carbon Nano Onion Supported Co-Pt Alloy Catalysts

Huiyu Li[1] · Bin Zhang[1] · Yiqing Jiang[1] · Yanhui Song[1,2] · Xinliang Feng[3] · Peizhi Liu[1] · Junjie Guo[1]
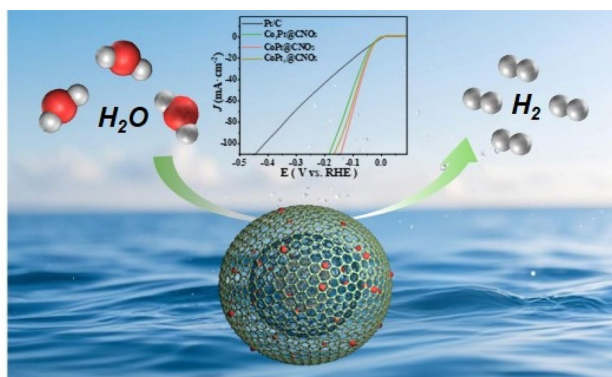
Abstract

Although commercial Pt/C catalyst is currently the preferred catalyst for hydrogen evolution reaction (HER) at the cathode of a water electrolyzer, large-scale applications in the prospective industries are still constrained severely by its high cost and insufficient durability. Therefore, developing a highly active, pH-universal, low-cost, and robust HER electrocatalyst is a key aspect for promoting the application of green hydrogen energy, but challenging. In this work, highly defective graphene nanospheres were prepared by arc discharge in toluene, and then annealed to form carbon nano onions (CNOs). Three catalysts with excellent pH-universal activities and stabilities, $CoPt_3@CNOs$, $CoPt@CNOs$, $Co_3Pt@CNOs$, were then prepared by loading Co-Pt alloys with various phases on CNOs using microwave hydrothermal method. Structural characterizations revealed that the uniformly distributed CoPt alloy nanoparticles with an average size of 2.78 nm, the proper bonding between Co and Pt, and the strong confinement effect of CNOs substrate for CoPt nanoparticles brought CoPt@CNOs with optimized HER performance, which is even better than that of commercial Pt/C catalysts. CoPt@CNOs required low overpotentials of 33, 36 and 26 mV at a current density of 10 mA cm^{-2}, and 132, 128 and 43 mV at 100 mA cm^{-2} in 1 M KOH, 1 M PBS, and 0.5 M H_2SO_4, respectively. In addition, the CoPt@CNOs showed excellent stability over the full pH range. More importantly, the Pt content in CoPt@CNOs was only 9.75 wt%, which reduced more than one half compared with 20 wt% in commercial Pt/C catalysts. This study presents an easy and economical approach to fabricate high-efficiency and pH-universal HER catalysts, which provides a great promise for the commercial use of green hydrogen.

Graphical Abstract

Keywords Carbon nano onions · Hydrogen evolution reaction catalyst · Co-Pt alloy nanoparticles · pH-universal

---

H. Li and B. Zhang are contributed equally to this work.

Extended author information available on the last page of the article

Abbreviations

HER	Hydrogen evolution reaction
DFT	Density functional theory
CNOs	Carbon nano onions
XRD	X-ray diffraction
SEM	Scanning electron microscope
EDS	Energy dispersive spectrometer
TEM	Transmission electron microscope
HRTEM	High-resolution transmission electron microscope
XPS	X-ray photoelectron spectroscopy
ICP-OES	Inductively coupled plasma optical emission spectrometer
SCE	Saturated calomel electrode
GCE	Glassy carbon electrode
PBS	Phosphate buffered saline
LSV	Linear sweep voltammetry
CV	Cyclic voltammetry
EIS	Electrochemical impedance spectroscopy
R_{ct}	Charge transfer resistance
ECSA	Electrochemical active surface area
C_{dl}	Electrochemical double-layer capacitance
SAED	Selected area electron diffraction

1 Introduction

As a clean energy vector with the highest energy density among fuels and zero carbon emissions, hydrogen represents a viable pathway to address both the energy scarcity challenge and climate change concerns [1]. Electrochemical water splitting represents an efficient technological approach for high-purity hydrogen production [2]. High-performance electrocatalysts demonstrate remarkable capability in reducing the overpotential required for the hydrogen evolution reaction (HER) during the water electrolysis, thereby substantially enhancing the overall catalytic kinetics and reaction efficiency [3]. The operational pH range of most reported electrocatalysts remains limited, as HER reaction pathways are strongly influenced by H^+ and OH^- concentrations. What is more, the localized pH fluctuations occurring at the electrode-electrolyte interface during prolonged water splitting undermine the energy efficiency of electrolysis [4]. Thus, an optimal electrocatalyst should maintain superior activity across various electrolyte environments. Despite being the commercial electrocatalyst, Pt/C catalysts face significant challenges in widespread implementation due to their poor durability and high-cost [5]. Thus, the development of broad pH-range catalysts outperforming Pt/C in HER activity remains an urgent research priority.

Significant attention has been directed toward earth-abundant non-precious transition metal-based electrocatalysts,

demonstrating promising HER performance and cost-effectiveness [6]. Although highly reactive d-electrons of non-precious transition metals facilitates effective H-O bond cleavage, their stability are relatively low, especially in an acid environment. Therefore, the formation of ordered intermetallic compounds through Pt alloying with non-precious transition metals represents a promising approach to improve catalytic activity, stability, and reduce production costs [5]. Numerous intermetallic Pt–M alloys, including Pt_3Fe [7], PtFe [8], Pt_3Co [9], PtCo [10], etc., have been reported to exhibit excellent electrocatalytic activity for HER. Random solid solution of Pt-Co nanoparticles supported on carbon nano onions (CNOs) have also been developed as outstanding pH-universal HER catalysts in our previous work [11]. However, only ~10% Pt was substituted by Co, and the Pt loading was not significantly reduced. Density functional theory (DFT) analyses demonstrate that transition metal dopants induce electronic structure modifications through enhanced d-orbital coupling, causing Pt d-band center shifts and optimized adsorption energies of hydrogen intermediates, and thereby boosting catalytic efficiency. Therefore, ordered structure Pt-M catalysts alloying with more non-precious metal are highly probable and imperative.

What is more, thanks to the satisfactory conductivity, tunability of the structural and physicochemical properties, carbon-based materials have shown great promise as substrates of HER catalysts [12]. In prior research, CNOs composed of defective graphene layers have been developed as an excellent catalyst substrate. The CNOs supported catalysts exhibited enhanced electrocatalytic performance owing to their high specific surface area, superior electron transport characteristics, and secure nanoparticle immobilization capabilities [13, 14]. Generally, alloy catalysts need to be synthesized through high-temperature annealing to overcome the kinetic energy barrier of atomic ordering and promote the formation of intermetallic alloy compounds. Su and co-works showed that defects in carbon materials contributed to the alloying of Pt and Co atoms [15]. Therefore, we propose to anchor Pt and Co atoms on CNOs with a higher defect density, promoting their alloying to form ordered intermetallic compounds.

Herein, we synthesized highly defective CNOs via an improved arc-discharge technique in liquid toluene, and then annealed in a tube furnace. Co_xPt_y@CNOs electrocatalysts were synthesized from loading Co-Pt alloy nanoparticles on CNOs by a microwave hydrothermal method. The Co-Pt alloys with different phases have been achieved by changing the atomic ratio of Pt and Co source. The prepared CoPt@CNOs catalyst exhibited outstanding HER properties in pH-universal media. This research provides a simple and economical solution for the development of pH-universal

HER catalysts, which in turn will facilitate the practical applications of hydrogen energy conversions.

2 Experimental

2.1 Preparation of the Catalyst

The preparation of Co_xPt_y@CNOs catalysts is illustrated as Fig. 1. As described in previous research [13, 14], CNOs were obtained via an improved arc-discharge technique in liquid toluene, and then subjected to anneal in a tube furnace. Under Ar atmosphere, they were heated at a rate of 10 °C min^{-1} up to 1000 °C and held at this temperature for 2 h. The obtained CNOs were further used as catalyst supports to synthesize Co_xPt_y@CNOs through a microwave hydrothermal method. Typically, CNOs (50 mg), $C_{10}H_{14}O_4Pt$ (39 mg), $(CH_3COO)_2Co \cdot 4H_2O$ (8.3 mg) and $C_{16}H_{33}(CH_3)_3NBr$ (141.9 mg) were dissolved in 50 mL DMF under ultrasonication to prepare a mixture ($C_{10}H_{14}O_4Pt$ at 2 mmol/L, $(CH_3COO)_2Co \cdot 4H_2O$ at 0.7 mmol/L, $C_{16}H_{33}(CH_3)_3NBr$ at 8 mmol/L). Subsequently, the blend was poured into an autoclave (100 mL) and processed in a microwave reactor. The airtight autoclave was heated with a rate of 10 °C min^{-1} up to 200 °C and the temperature was held at 200 °C for 1 h. During this period, continuous magnetic stirring was applied to ensure uniform reaction conditions. Ultimately, the target product was obtained through rinsing with C_2H_6O for 5 times and then being dried at 60 °C for 6 h, and the products were designated as $CoPt_3$@CNOs. The synthesis conditions for CoPt@CNOs and Co_3Pt@CNOs were identical to those for $CoPt_3$@CNOs with the exception of the amount of $(CH_3COO)_2Co \cdot 4H_2O$, which was modified to 2 mmol/L and 6 mmol/L, respectively.

2.2 Catalyst Characterization

X-ray diffraction (XRD) studies were taken on a multipurpose X-Ray Diffractometer (Ultima IV, Rigaku, Japan. $Cu_{K\alpha}$ radiation, $\lambda = 1.5418$ Å, Rated tube voltage 40 kV and Rated tube current 40 mA). Scanning electron microscope (SEM, TESCAN, LYRA3 XMH) equipped with energy dispersive spectrometer (EDS, Oxford Instruments, X-Max^N) and high-resolution transmission electron microscope (HRTEM, JEOL, JEM-2010) were employed to characterize microstructures of the obtained samples. X-ray photoelectron spectroscopy (XPS) was performed on an X-ray photoelectron spectrometer (Escalab 250Xi, Thermo Fisher Scientific, USA). Inductively coupled plasma optical emission spectrometer (ICP-OES, 720, Agilent, USA) was used to detect the metal content of the catalyst.

2.3 Electrochemical Measurement

Electrochemical experiments were conducted using a working station (CHI 760E, Chenhua Instrument Factory, China) equipped with a conventional three-electrode system. The graphite rod electrode and saturated calomel electrode
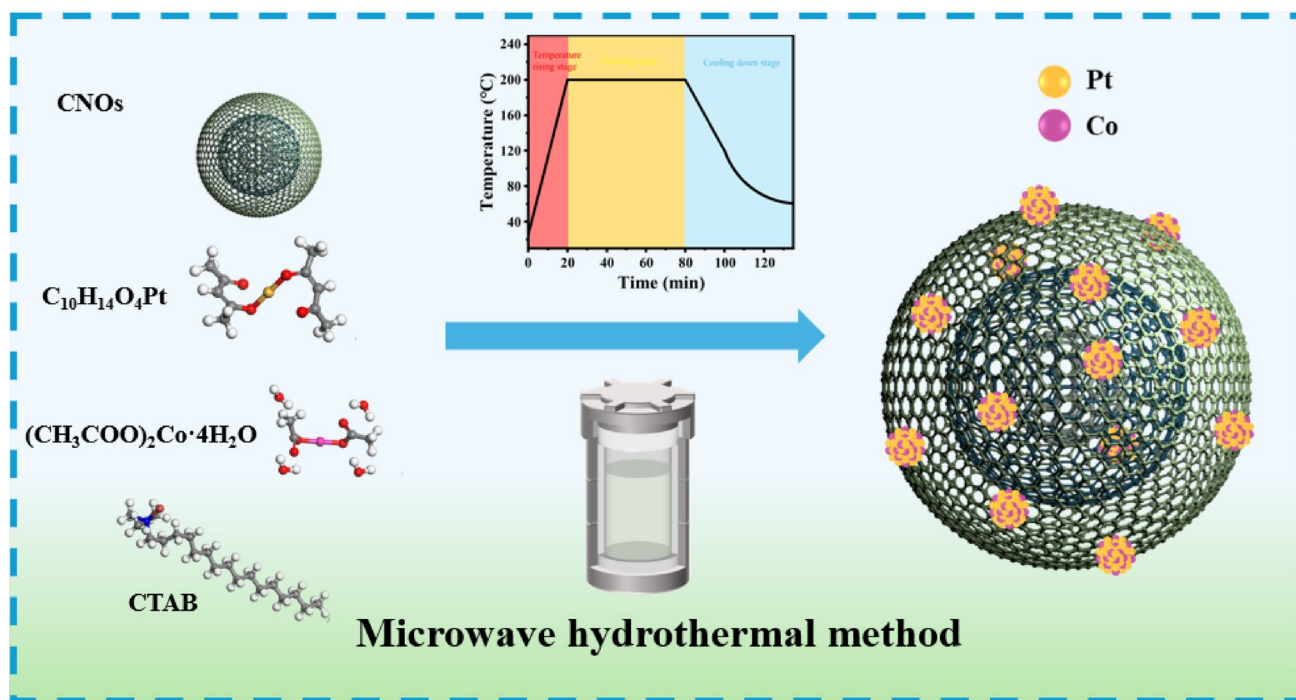

Fig. 1 Schematic illustration for the synthesis of Co_xPt_y@CNOs catalysts

(SCE) were employed as the counter and reference electrode. A glassy carbon electrode (GCE) (3 mm diameter, 0.071 cm^2) served as the working electrode. Prior to the electrochemical experiments, the GCE was polished with Al$_2$O$_3$ powders. Meanwhile, the electrolyte was degassed by bubbling argon through it for an hour at room temperature. Catalyst ink preparation involved ultrasonically dispersing 2 mg of active material in a 1:1 ethanol/water mixture (380 μL in total) with 20 μL Nafion binder (5 wt%) for 30 min to ensure homogeneous electrode fabrication. A precisely controlled 1.4 μL aliquot of catalyst ink was deposited onto the polished glassy carbon electrode, achieving a uniform loading density of 0.1 mg cm^{-2}, followed by an air-drying prior to electrochemical characterization. The experiments were carried out in 0.5 M H$_2$SO$_4$, 1 M phosphate buffered saline (PBS), and 1 M KOH solutions, respectively. Linear sweep voltammetry (LSV) was carried out under a scan rate of 5 mV s^{-1}, and the polarization curves were corrected by 95% iR compensation. The potential measured against a SCE electrode (E (vs. SCE)) was converted to the potential against a reversible hydrogen electrode (E (vs. RHE)), and the conversion formula is:

$$E\,(v\,s\,RHE) = E\,(v\,s\,SCE) + 0.2438\,V + 0.0591\,V \times pH \qquad (1)$$

The Tafel slope were derived from the LSV curve. Electrochemical impedance spectroscopy (EIS) was performed in a frequency range from 0.01 Hz to 100 kHz with an AC amplitude of 5 mV. To assess the electrochemical active surface area (ECSA), the electrochemical double-layer capacitance (C$_{dl}$) was measured within a limited potential window. This measurement was achieved via cyclic voltammetry (CV) at scan rates of 20, 40, 60, 80, and 100 mV s^{-1}. The ECSA value is calculated from the equation:

$$ECSA = \frac{C_{dl}}{C_s} \qquad (2)$$

Where C$_s$ is the specific capacitance of an ideal electrode with a smooth surface, and an average value of 0.04 mF cm^{-2} is usually adopted [16, 17].

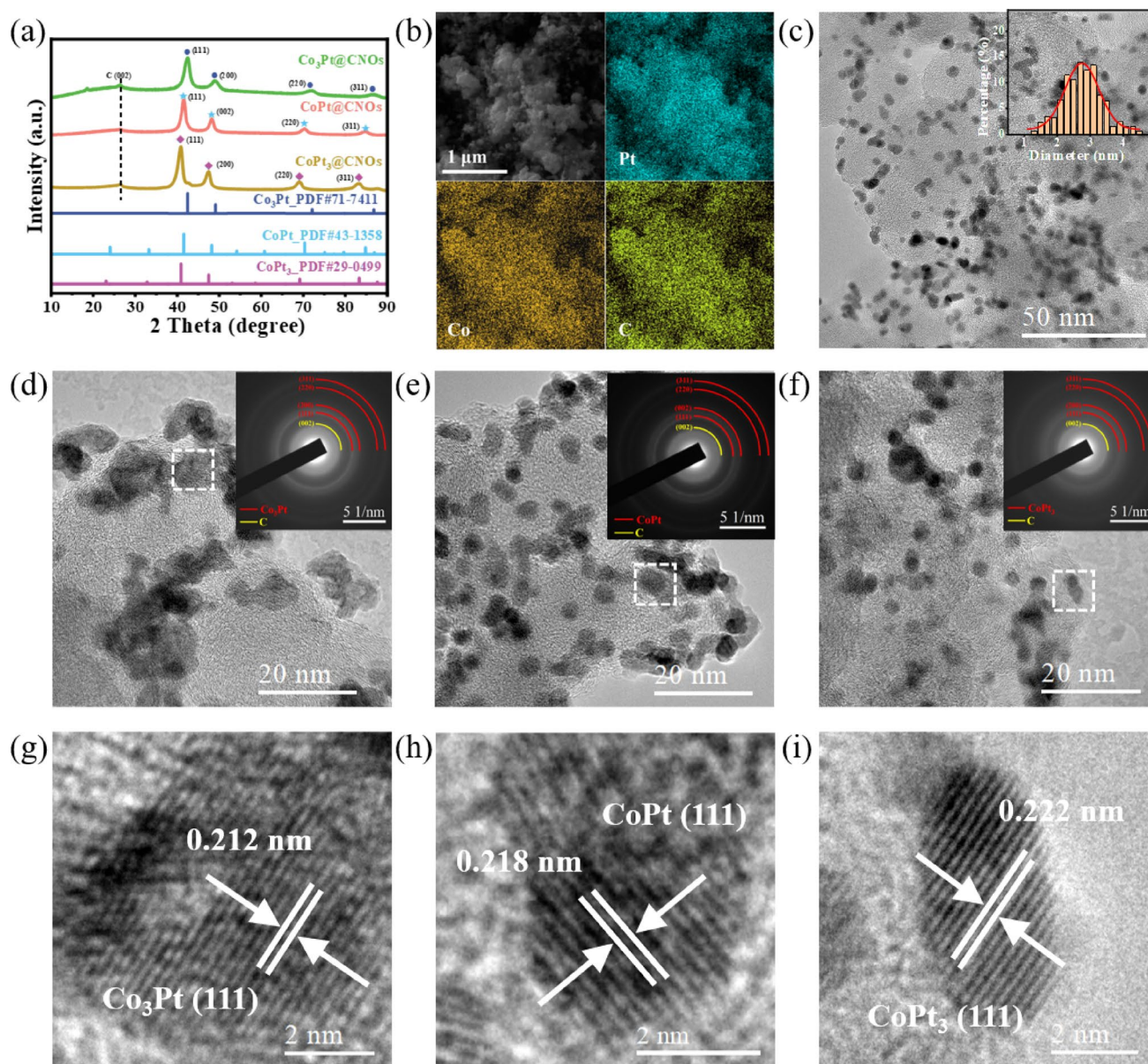## 3 Results and Discussion

3.1 Structure and Architecture of Co$_x$Pt$_y$@CNOs

XRD, SEM, and HRTEM were used to comprehensively describe the microstructures of the as-synthesized Co$_3$Pt@CNOs, CoPt@CNOs, and CoPt$_3$@CNOs The diffraction feature at 26.4° in XRD pattern (Fig. 2a) corresponds to the (002) crystal plane of graphite (PDF#41-1487), while other sharp peaks in the synthesized Co$_3$Pt@CNOs, CoPt@CNOs and CoPt$_3$@CNOs catalysts are in perfect agreement with the standard PDF of Co$_3$Pt (PDF#71-7411), CoPt (PDF#43-1358) and CoPt$_3$ (PDF#29–0499) [18, 19]. CoPt@CNOs elemental mapping has been carried out using SEM and EDS, as illustrated in Fig. 2b. The particles in CoPt@CNOs powder have a spherical morphology, with uniformly dispersed Pt (cyan), Co (orange), and C (sallow). Co$_3$Pt@CNOs (Fig. S1a–c) and CoPt$_3$@CNOs (Fig. S1d–f) exhibit the same configuration. As shown in Fig. 2c, TEM analysis revealed the size distribution profile of CoPt alloy nanoparticles in CoPt@CNOs. The findings suggest that the synthesized CoPt nanoparticles have an average diameter of 2.78 nm and are evenly distributed on the CNOs. In addition, similar results are displayed for Co$_3$Pt@CNOs (Fig. S2a, b) and CoPt$_3$@CNOs (Fig. S2c, d). The average size of Co$_3$Pt alloy nanoparticles in Co$_3$Pt@CNOs is 3.01 nm, and average size of CoPt$_3$ in CoPt$_3$@CNOs is 2.69 nm.

Figure 2d shows the HRTEM image of Co$_3$Pt@CNOs, and the inset is the corresponding selected area electron diffraction (SAED) pattern. The SAED diffraction rings correspond to the (002) crystal planes of C and (111), (200), (220), (311) crystal planes of Co$_3$Pt from inner to outside, respectively [20, 21]. Figure 2g shows a magnified image of the dashed box in Fig. 2d, where the lattice stripes spacing at 2.12 Å correspond to the Co$_3$Pt (111) faces. Figure 2e shows the HRTEM image of CoPt@CNOs with the inserted SAED pattern corresponding to the C (002), CoPt (111), CoPt (002), CoPt (220) and CoPt (311) crystallographic facets from inside to outside, respectively. The dashed box area in Fig. 2e, where the lattice stripes of 2.18 Å match the CoPt (111) faces, is magnified in Fig. 2h. In Fig. 2f, the HRTEM image of CoPt$_3$@CNOs is displayed, featuring an inset of the corresponding SAED pattern. The rings ranging from the innermost to the outermost signify the (002) crystal planes of C and the (111), (200), (220), (311) crystal planes of CoPt$_3$ alloy, respectively. Additionally, Fig. 2i offers a magnified view of the CoPt$_3$ nanoparticles outlined by the dashed box in Fig. 2f, where the lattice stripes of 2.22 Å correspond to the CoPt$_3$ (111) faces [22, 23].

In addition, as the Raman spectra shown in Fig. S3, the defective graphene layers in CNOs prepared by the arc discharge in toluene held a much larger I$_D$/I$_G$ ratio of ~0.83 than that of 0.45 produced from the high-purity graphite electrodes during arc discharge [11]. The larger I$_D$/I$_G$ ratio means a higher defect density in the graphene layers, which is beneficial for the forming and anchoring of ordered Pt-Co alloy nanoparticles [15], and mass transfer during the HER process. ICP-OES was used to determine the metal contents of the catalysts, and the findings are shown in Table S1 and S2. The atomic percentages of Pt and Co further confirm that the physical phases of the synthesized alloys are Co$_3$Pt,
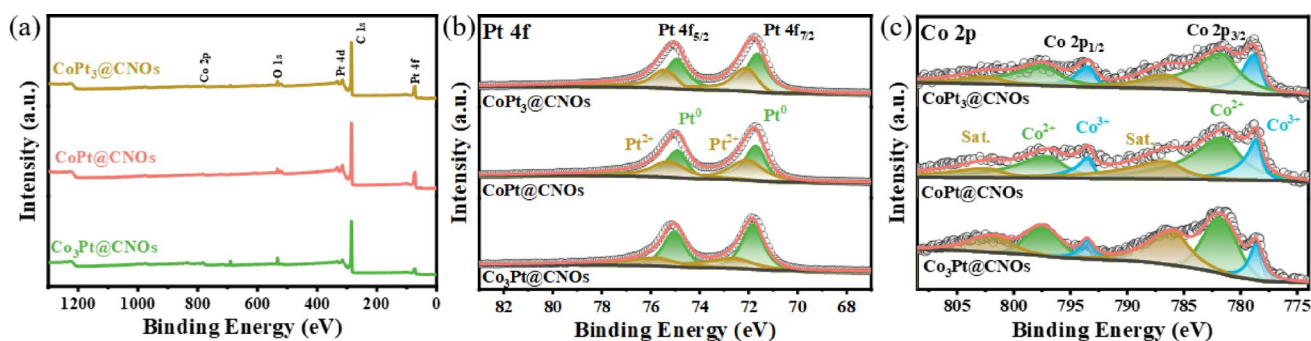
Fig. 2 **a** XRD patterns of $Co_3Pt@CNOs$, $CoPt@CNOs$ and $CoPt_3@CNOs$; **b** SEM diagrams of $CoPt@CNOs$ and corresponding EDS element distributions; **c** TEM image of $CoPt@CNOs$, and the inserted histogram is a statistical diagram of the particle size distribution of CoPt and $CoPt_3$, in accordance with the XRD and TEM CoPt alloy; **d**–**f** HRTEM images and corresponding SAED patterns of $Co_3Pt@CNOs$, $CoPt@CNOs$, $CoPt_3@CNOs$, respectively; **g**–**i** an enlarged view of the selected area marked with the dash box in **d**–**f**, respectively
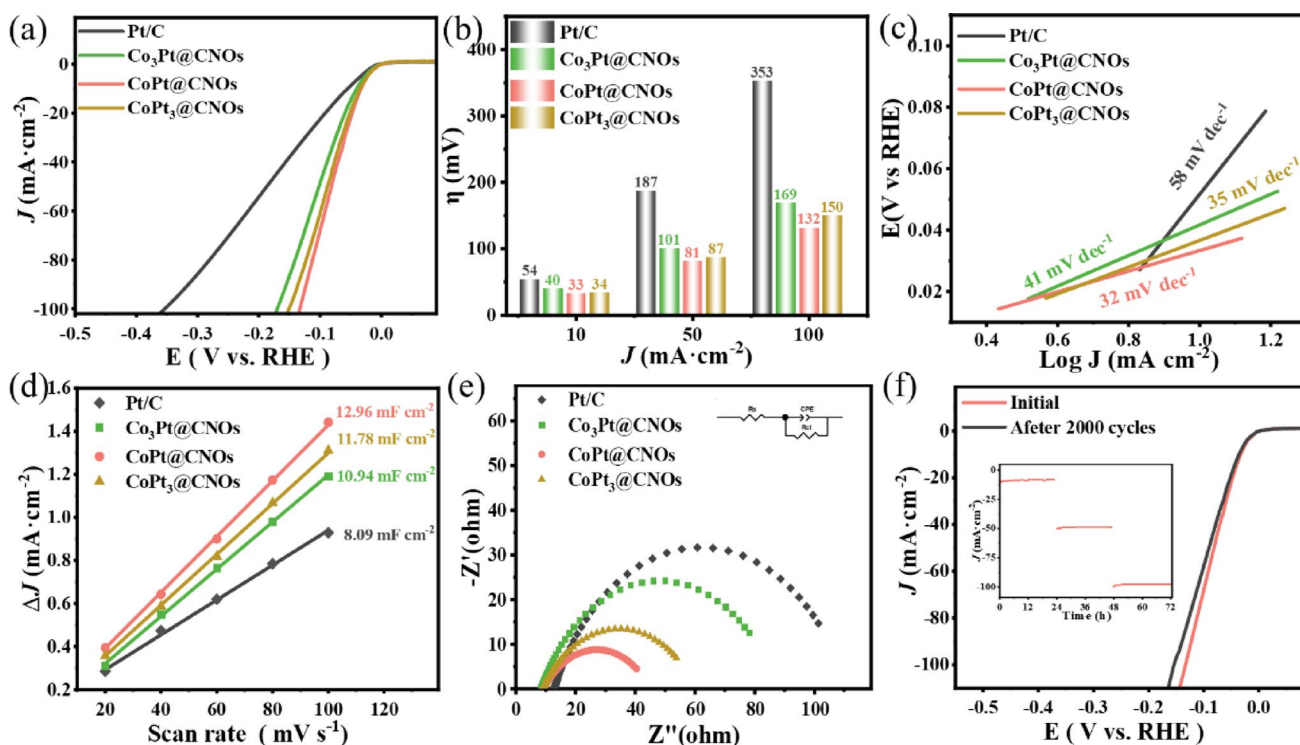
results. What is more, $Co_3Pt@CNOs$ contained 10.53 wt% Pt, $CoPt@CNOs$ contained 9.75 wt% Pt, and $CoPt_3@CNOs$ contained 10.13 wt% Pt. That is, the $Co_xPt_y@CNOs$ electrocatalysts halve the Pt content compared to commercial Pt/C catalysts.

The catalysts were characterized by XPS to investigate the bonding state of the surface atoms. The survey spectra (Fig. 3a) indicate the presence of Pt, Co, C and a touch of O elements in the catalyst, which is consistent with the EDS results. To determine the chemical state of Co-Pt

nanoparticles in $Co_xPt_y@CNOs$ catalyst, the deconvoluted XPS spectra of Pt 4f were illustrated in Fig. 3b. The deconvoluted Pt $4f_{7/2}$ and $4f_{5/2}$ peaks can be resolved into two distinct states: metallic Pt^0 species and oxidized Pt^{2+} states, and the latter attributed to a surface oxidation process [11]. The deconvoluted Co 2p XPS spectrum (Fig. 3c) reveals characteristic spin-orbit doublets of $2p_{1/2}$ and $2p_{3/2}$ states [24]. Each component can be further resolved into distinct peaks representing Co^{2+}, Co^{3+}, along with a satellite peak (Sat.), respectively. The binding energy values associated with different chemical states of Pt and Co in the catalysts are

Fig. 3 **a** Survey XPS spectra of CoPt$_3$@CNOs, CoPt@CNOs and Co$_3$Pt@CNOs; **b**, **c** spectra XPS spectra of Pt 4f and Co 2p in CoPt$_3$@CNOs, CoPt@CNOs and Co$_3$Pt@CNOs, respectively

Fig. 4 HER performance characterization in 1 M KOH: **a** LSV curves of Co$_3$Pt@CNOs, CoPt@CNOs, CoPt$_3$@CNOs and Pt/C; **b** Visualized comparison among HER overpotentials for η$_{10}$, η$_{50}$ and η$_{100}$; **c** Corresponding Tafel plots, **d** double layer capacitance plots, and **e** Nyquist plots; **f** LSV polarization curves of CoPt@CNOs electrocatalyst at ini-tial state and after 2000 CV cycles, with the inset of continuous stability test of CoPt@CNOs for every current density of 10, 50 and 100 mA cm^{-2} under the corresponding overpotential of 33, 81 and 132 mV by chronoamperometry

summarized as Table S3 and S4. It is obvious that the Pt 4f and Co 2p binding energies of the CoPt@CNOs shift nega-tively compared with that of the Co$_3$Pt@CNOs and CoPt$_3$@CNOs, which means less oxidized Pt and Co exist in the CoPt@CNOs [25, 26]. In addition, this negative shift can tune the Pt−Pt distances and the transfer of electrons from Pt to Co, and thus reduce the adsorption Gibbs free energy of H*. So the HER performance of CoPt@CNOs is better than that of Co$_3$Pt@CNOs and CoPt$_3$@CNOs [27, 28, 29].

3.2 Electrochemical Measurements of Co$_x$Pt$_y$@CNOs

The electrocatalytic performance of synthesized materi-als was evaluated across various pH conditions employing a conventional three-electrode system. The performance of all three carbon-supported nano-alloy catalysts (Fig. 4) is far superior to that of Pt/C, while CoPt@CNOs exhib-its the most outstanding catalytic performance in alkaline electrolyte. The LSV curves (Fig. 4a) demonstrate HER overpotentials of Pt/C, Co$_3$Pt@CNOs, CoPt@CNOs, and CoPt$_3$@CNOs in 1 M KOH. The visualized comparison
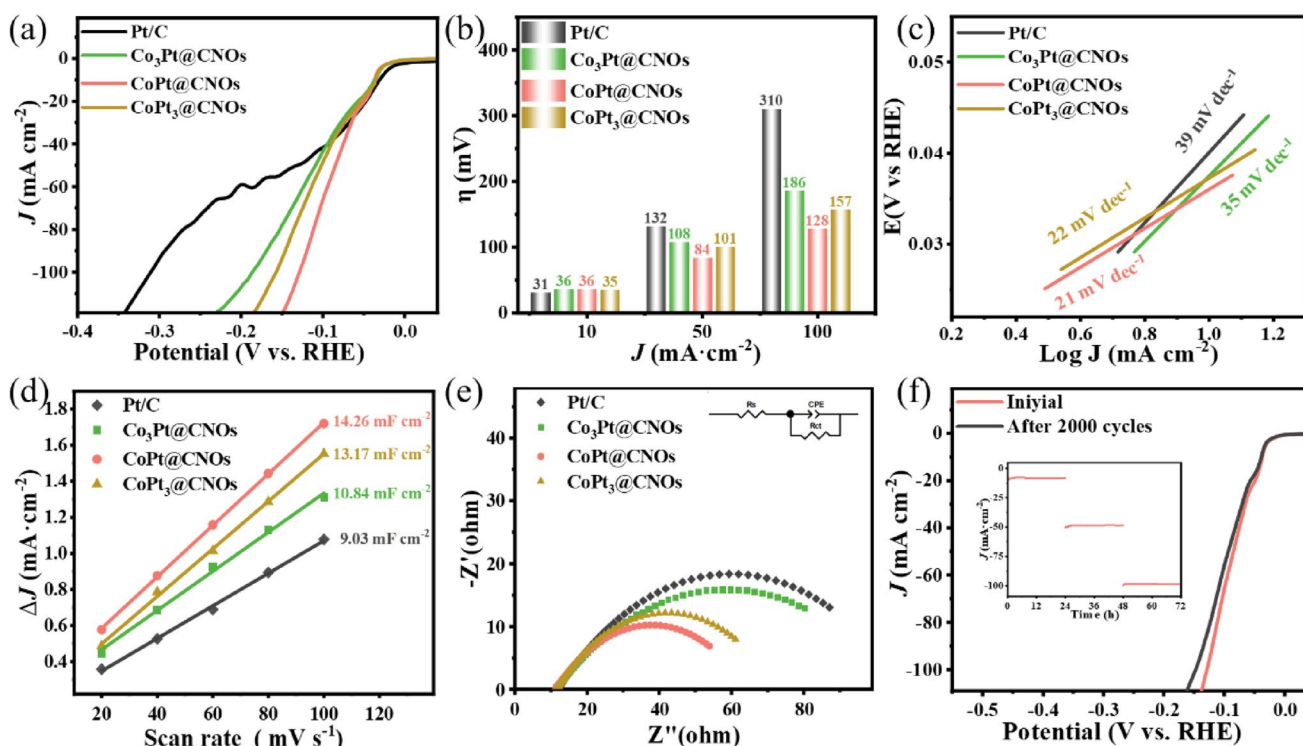
(Fig. 4b) demonstrates significantly reduced overpotentials of Co_xPt_y@CNOs among the catalysts: the overpotential of Pt/C is 54 mV, while Co_3Pt@CNOs, CoPt@CNOs and $CoPt_3$@CNOs show reduced overpotentials of 40, 33 and 34 mV at 10 mA cm^{-2}, respectively. This trend continues at higher current densities, with corresponding overpotentials of 187, 101, 81 and 87 mV at 50 mA cm^{-2}, and 353, 169, 132 and 150 mV at 100 mA cm^{-2}. As presented in Fig. 4c, the Tafel slopes corresponding to Co_xPt_y@CNOs and Pt/C are depicted. The comparative Tafel slopes analysis reveals promoted reaction kinetics for CoPt@CNOs (32 mV dec^{-1}) compared to Pt/C (58 mV dec^{-1}), Co_3Pt@CNOs (41 mV dec^{-1}), and $CoPt_3$@CNOs (35 mV dec^{-1}) [30]. As presented in Fig. 4d, the electrochemical C_{dl} of Pt/C, Co_3Pt@CNOs, CoPt@CNOs and $CoPt_3$@CNOs were investigated through CV in 1 M KOH, with potential scanning between 0.76 and 0.86 V, from which the ECSA of the catalysts was assessed. CoPt@CNOs exhibits the highest C_{dl} value of 12.96 mF cm^{-2} and the largest ECSA value of 324 (Table S5), which strongly implies the presence of a larger number of exposed active sites in CoPt@CNOs. This finding aligns with the outcomes of the electrocatalytic activity tests. EIS was employed to investigate the HER kinetics of the catalyst as well. Remarkably, the Nyquist plots in Fig. 4e reveals that CoPt@CNOs exhibits remarkably lower charge transfer resistance (R_{ct}) relative to Pt/C and other Co_xPt_y@CNOs. In fact, when compared with other catalysts, CoPt@CNOs demonstrates the lowest R_{ct} in various pH conditions, as presented in Table S6, which indicates the most efficient charge transfer rate and the optimal electrical conductivity. Figure 4f shows the stability of CoPt@CNOs electrocatalysts. Accelerated stability testing through 2000 CV cycles demonstrated negligible activity reduction for CoPt@CNOs, with overpotential increases of merely 3, 8 and 18 mV at 10, 50 and 100 mA cm^{-2}, respectively. This indicates a remarkable edge in stability compared to the Pt/C catalyst [31]. Moreover, the prepared CoPt@CNOs also demonstrates superior continuous stability with a disregard drop of current for a chronoamperometry test lasting 24 h for every current density of 10, 50 and 100 mA cm^{-2} respectively (inset). This indicates that the CoPt@CNOs catalyst has excellent cyclic and continuous stability. HRTEM (Fig. S7) was further used to inspect the micromorphology of CoPt@CNOs following the HER stability test. No apparent structural disintegration and particle agglomeration were detected. Actually, CoPt@CNOs represents the same behavior after stability tests in acidic and neutral environments.

Motivated by the significance of neutral electrolyte during application, the catalytic performance of Co_xPt_y@CNOs electrode for HER in PBS was also explored. Unsurprisingly, the Co_xPt_y@CNOs electrode exhibits outstanding HER activity in 1 M PBS. Electrochemical performance analysis in Fig. 5a, b reveals CoPt@CNOs exceptional catalytic efficiency, displaying markedly reduced overpotentials across tested current densities. At 10 mA cm^{-2}, the overpotential achieves 36 mV, closely matching Co_3Pt@CNOs (36 mV), $CoPt_3$@CNOs (35 mV), and Pt/C (31 mV). The performance divergence becomes pronounced at elevated current densities, where CoPt@CNOs maintains 84 mV at 50 mA cm^{-2} and 128 mV at 100 mA cm^{-2}, significantly lower than that of Pt/C (132 mV, 310 mV), Co_3Pt@CNOs (108 mV, 186 mV), and $CoPt_3$@CNOs (101 mV, 157 mV) under equivalent conditions. Figure 5c demonstrates the derived Tafel slopes from the LSV curves. Evidently, CoPt@CNOs displays a Tafel slope of 21 mV dec^{-1}. This value is lower than that of Pt/C (39 mV dec^{-1}), Co_3Pt@CNOs (35 mV dec^{-1}), and $CoPt_3$@CNOs (22 mV dec^{-1}), demonstrating its more positive reaction kinetics during the electrochemical process. The C_{dl} (Fig. 5d) of Pt/C, Co_3Pt@CNOs, CoPt@CNOs and $CoPt_3$@CNOs were investigated through CV in 1 M PBS while the potential was scanned from 0.76 to 0.86 V. Specifically, CoPt@CNOs exhibits the highest C_{dl} value of 14.26 mF cm^{-2}. This corresponds to the largest ECSA value of 356.5 (Table S5), which strongly suggests that CoPt@CNOs possess a larger quantity of exposed active sites in HER [32]. As shown in Fig. 5e, the Nyquist plot also displays that CoPt@CNOs has the lowest R_{ct} when contrasted with Pt/C, Co_3Pt@CNOs and $CoPt_3$@CNOs, indicating the most efficient charge transfer rate. Figure 5f illustrates the CV cycle stability and a chronoamperometry test lasting 24 h for every current density of 10, 50 and 100 mA cm^{-2} of CoPt@CNOs electrocatalysts. Along with a continuous stability test, it's clearly evident that the potential shows no obvious deterioration, demonstrating the outstanding mass transfer characteristics and long-term durability of the CoPt@CNOs. In addition, stability test through 2000 CV cycles demonstrates negligible performance reduction for CoPt@CNOs, with overpotential increases of merely 3, 11, and 19 mV at current densities of 10, 50, and 100 mA cm^{-2}, respectively, indicating outstanding durability compared to the Pt/C catalyst.
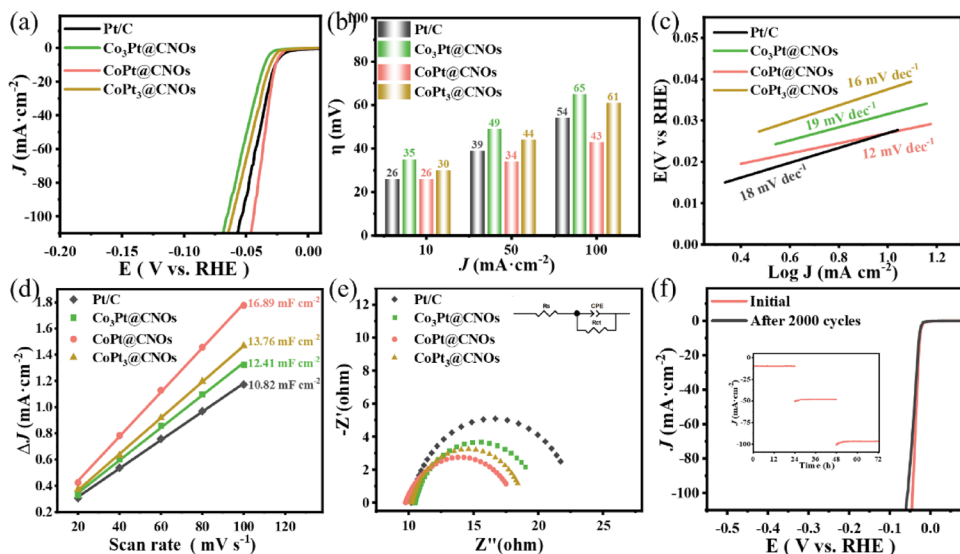
The HER activity exhibited by the Pt/C catalyst within acidic conditions is markedly more prominent than that observed in alkaline and neutral conditions, which discrepancy can be principally ascribed to the significantly elevated concentration of H^+. At the same time, acidic environments place higher demands on the stability of alloy catalysts. Thus, the catalytic performance of the synthesized alloy catalysts was examined in an acidic medium of 0.5 M H_2SO_4. As presented in Fig. 6a, b, CoPt@CNOs needs only 26 mV overpotential to reach 10 mA cm^{-2}, which is less than that of Co_3Pt@CNOs (35 mV) and $CoPt_3$@CNOs (30 mV). Significantly, at a current density of 50 mA cm^{-2}, the HER activity of CoPt@CNOs exceeds that of the Pt/C

Fig. 5 HER performance characterization in 1 M PBS: **a** LSV curves of Co$_3$Pt@CNOs, CoPt@CNOs, CoPt$_3$@CNOs and Pt/C; **b** Visualized comparison among HER overpotentials for η_{10}, η_{50} and η_{100}; **c** Corresponding Tafel plots; **d** double layer capacitance plots; **e** Nyquist plots; **f** LSV polarization curves of CoPt@CNOs electrocatalyst at initial state and after 2000 CV cycles, with the inset of continuous stability test of CoPt@CNOs for every current density of 10, 50 and 100 mA cm^{-2} under the corresponding overpotential of 36, 84 and 128 mV by chronoamperometry

Fig. 6 HER performance characterization in 0.5 M H$_2$SO$_4$: **a** LSV curves of Co$_3$Pt@CNOs, CoPt@CNOs, CoPt$_3$@CNOs and Pt/C; **b** Visualized comparison among HER overpotentials for η_{10}, η_{50} and η_{100}; **c** Corresponding Tafel plots; **d** double layer capacitance plots; **e** Nyquist plots. **f** LSV polarization curves of CoPt@CNOs electrocatalyst at initial state and after 2000 CV cycles, with the inset of continuous stability test of CoPt@CNOs for every current density of 10, 50 and 100 mA cm^{-2} under the corresponding overpotential of 26, 34 and 43 mV by chronoamperometry

catalyst. CoPt@CNOs shows a Tafel slope (Fig. 6c) of 12 mV dec^{-1}, which is lower than that of Pt/C (18 mV dec^{-1}), Co$_3$Pt@CNOs (19 mV dec^{-1}), and CoPt$_3$@CNOs (16 mV dec^{-1}), demonstrating the greatly improved reaction kinetics of CoPt@CNOs. In a 0.5 M H$_2$SO$_4$ solution, CV curves of Pt/C, CoPt@CNOs, Co$_3$Pt@CNOs and CoPt$_3$@CNOs were recorded while the potential was scanned from 0.85

to 0.95 V. CoPt@CNOs exhibits the highest C$_{dl}$ value of 16.89 mF cm^{-2}. This corresponds to the largest ECSA value of 422.25 (Table S5), which strongly suggests that CoPt@CNOs possesses a larger quantity of exposed active sites in HER. The Nyquist plots in Fig. 6e reveals that CoPt@CNOs exhibits significantly lower R$_{ct}$ relative to Pt/C and other Co$_x$Pt$_y$@CNOs, suggesting optimal electron transfer

kinetics. Figure 6f demonstrates the outstanding stability and activity of CoPt@CNOs after CV cycling and continuous stability measurement in acidic medium.

4 Conclusion

In conclusion, nano-alloy catalysts with different Co:Pt ratios loaded on carbon nano onions, $Co_3Pt@CNOs$, CoPt@CNOs, and $CoPt_3@CNOs$, were successfully prepared by a microwave hydrothermal method, and the effects of nanoparticle phases on the HER properties were studied. All of them exhibited better HER activity and durability than commercial 20 wt% Pt/C catalyst in the pH-universal range, with CoPt@CNOs behaving the best performance: overpotentials of 33 mV@10 mA cm^{-2}, 81 mV@50 mA cm^{-2}, 132 mV@100 mA cm^{-2} in alkaline, 36 mV@10 mA cm^{-2}, 84 mV@50 mA cm^{-2}, 128 mV@100 mA cm^{-2} in neutral, and 26 mV@10 mA cm^{-2}, 34 mV@50 mA cm^{-2}, 43 mV@100 mA cm^{-2} in acidic media. The CoPt alloy has an average particle size of 2.78 nm and is uniformly anchored to the CNOs. The formation of ordered phases of Co-Pt alloy nanoparticles modulates the electronic structure of the catalysts, and the outstanding charge-mass transport property of the CNOs matrix are all favorable for the improvement of HER activity, while the Pt concentration has been reduced by half. The stability of the catalyst is also improved due to the robust interaction between the alloy nanoparticles and the defective graphene framework of CNOs. This study provides a new direction for the synthesis of novel catalysts for water electrolysis in pH-universal range with greatly reduced noble-metal loading, which reserves a broad potential in commercial applications.

Author Contributions H L: Writing– original draft, Investigation, Methodology, Formal analysis, Data curation. B Z: Writing– original draft, Investigation, Methodology, Formal analysis, Data curation. Y J: Formal analysis, Data curation. Y S: Investigation, Funding acquisition. X F: Investigation, Supervision. P L: Writing– review and editing, Funding acquisition. J G: Writing– review and editing, Funding acquisition, Conceptualization. All authors reviewed the manuscript.

Declarations

Conflict of Interest The authors declare no competing interests.

Ethical Approval No tests on human participants or animals were performed by any of the authors, so the related considerations are not applicable.

Consent for Publication Not applicable.

References

1. Wu H, Huang Q, Shi Y et al (2023) Electrocatalytic water splitting: mechanism and electrocatalyst design. Nano Res 16:9142–9157. https://doi.org/10.1007/s12274-023-5502-8
2. Yan C, Liu Y, Zeng Q et al (2023) 2D nanomaterial supported Single-Metal atoms for heterogeneous photo/electrocatalysis. Adv Funct Mater 33:2210837. https://doi.org/10.1002/adfm.202210837
3. Wang C, Zhang Q, Yan B et al (2023) Facet engineering of advanced electrocatalysts toward hydrogen/oxygen evolution reactions. Nano-Micro Lett 15:52. https://doi.org/10.1007/s40820-023-01024-6
4. Yu Q, Fu Y, Zhao J et al (2023) Boron doping activate strong metal-support interaction for electrocatalytic hydrogen evolution reaction in full pH range. Appl Catal B 324:122297. https://doi.org/10.1016/j.apcatb.2022.122297
5. Kuang P, Ni Z, Zhu B et al (2023) Modulating the d-Band center enables ultrafine Pt_3Fe alloy nanoparticles for pH-Universal hydrogen evolution reaction. Adv Mater 35:2303030. https://doi.org/10.1002/adma.202303030
6. Liang L, Jin H, Zhou H et al (2021) Cobalt single atom site isolated Pt nanoparticles for efficient ORR and HER in acid media. Nano Energy 88:106221. https://doi.org/10.1016/j.nanoen.2021.106221
7. Qiao Y, Cui J, Qian F et al (2022) Pt_3Fe nanoparticles on B,N-Codoped carbon as oxygen reduction and pH-Universal hydrogen evolution electrocatalysts. ACS Appl Nano Mater 5:318–325. https://doi.org/10.1021/acsanm.1c03046
8. Zhong X, Wang L, Zhuang Z et al (2017) Double nanoporous structure with nanoporous PtFe embedded in graphene nanopores: highly efficient bifunctional electrocatalysts for hydrogen evolution and oxygen reduction. Adv Mater Inter 4:1601029. https://doi.org/10.1002/admi.201601029
9. Lin C, Huang Z, Zhang Z et al (2020) Structurally ordered Pt_3Co nanoparticles anchored on N-Doped graphene for highly efficient hydrogen evolution reaction. ACS Sustainable Chem Eng 8:16938–16945. https://doi.org/10.1021/acssuschemeng.0c06547
10. Zhang X-F, Meng H-B, Chen H-Y et al (2019) Bimetallic PtCo alloyed nanodendritic assemblies as an advanced efficient and robust electrocatalyst for highly efficient hydrogen evolution and oxygen reduction. J Alloys Compd 786:232–239. https://doi.org/10.1016/j.jallcom.2019.01.321
11. Zhang B, Peng D, Hao B et al (2024) One-step synthesis of carbon-onion-supported Pt Co alloy by underwater Arc discharge for pH-universal hydrogen evolution reaction. Sustainable Mater

Technol 42:e01160. https://doi.org/10.1016/j.susmat.2024.e0116 0

12. Wang J, Kong H, Zhang J et al (2021) Carbon-based electrocatalysts for sustainable energy applications. Prog Mater Sci 116:100717. https://doi.org/10.1016/j.pmatsci.2020.100717

13. Shen Y, Liu P, Du J et al (2020) Defect engineering in graphene-based nanospheres enhanced hydrogen evolution reaction performance of ruthenium nanoparticles. Carbon 166:388–395. https://doi.org/10.1016/j.carbon.2020.05.033

14. Yan X, Li H, Sun J et al (2018) Pt nanoparticles decorated high-defective graphene nanospheres as highly efficient catalysts for the hydrogen evolution reaction. Carbon 137:405–410. https://doi.org/10.1016/j.carbon.2018.05.046

15. Ji N, Sheng H, Liu S et al (2024) Boosting oxygen reduction in acidic media through integration of Pt-Co alloy effect and strong interaction with carbon defects. Nano Res 17:7900–7908. https://doi.org/10.1007/s12274-024-6774-3

16. Rafiq M, Harrath K, Feng M et al (2024) $Ni_x B/Mo_{0.8} B_3$ nanorods encapsulated by a Boron-Rich amorphous layer for universal pH water splitting at the ampere level. Adv Energy Mater 14:2402866. https://doi.org/10.1002/aenm.202402866

17. Xing M, Zhu S, Zeng X et al (2023) Amorphous/Crystalline $Rh(OH)_3$ /CoP heterostructure with hydrophilicity/ aerophobicity feature for All-pH hydrogen evolution reactions. Adv Energy Mater 13:2302376. https://doi.org/10.1002/aenm.202302376

18. Pan X, Yu S, Zhang J et al (2023) Universal Solid-Phase Seed-Mediated synthesis of monodisperse and ultrasmall $L1_0$ -PtM intermetallic nanocrystals. Chem Mater 35:2559–2568. https://doi.org/10.1021/acs.chemmater.2c03830

19. Gao Y, Uchiyama T, Yamamoto K et al (2023) Origin of high activity and durability of confined ordered intermetallic PtCo catalysts for the oxygen reduction reaction in rotating disk electrode and fuel cell operating conditions. ACS Catal 13:10988–11000. https://doi.org/10.1021/acscatal.3c01926

20. Wang Y, Zhang X, Liu Y et al (2012) Fabrication, structure and magnetic properties of $CoPt_3$, CoPt and Co_3 Pt nanoparticles. J Phys D: Appl Phys 45:485001. https://doi.org/10.1088/0022-3727/45/48/485001

21. Song Y, Kim D, Hong S et al (2023) Bimetallic synergy from a Reaction-Driven metal Oxide–Metal interface of Pt–Co bimetallic nanoparticles. ACS Catal 13:13777–13785. https://doi.org/10.1021/acscatal.3c03133

22. Zeng W-J, Wang C, Yan Q-Q et al (2022) Phase diagrams guide synthesis of highly ordered intermetallic electrocatalysts: separating alloying and ordering stages. Nat Commun 13:7654. https://doi.org/10.1038/s41467-022-35457-1

23. Okamoto H, Cu-Sb C-S, Pd-Ti F-NL-PN-S (2019) Si-Te Ta-V V-Zn J Phase Equilib Diffus 40:743–756. https://doi.org/10.1007/s11669-019-00760-w

24. Bai S, Huang B, Shao Q, Huang X (2018) Universal strategy for ultrathin Pt–M (M=Fe, Co, Ni) nanowires for efficient catalytic hydrogen generation. ACS Appl Mater Interfaces 10:22257–22263. https://doi.org/10.1021/acsami.8b05873

25. Shao X, Liang M, Kumar A et al (2022) Amorphization of metal nanoparticles by 2D twisted polymer for super hydrogen evolution reaction. Adv Energy Mater 12:2102257. https://doi.org/10.1002/aenm.202102257

26. Shao X, Liang M, Kim MG et al (2023) Density-Controlled metal nanocluster with modulated surface for pH-Universal and robust water splitting. Adv Funct Mater 33:2211192. https://doi.org/10.1002/adfm.202211192

27. Zhang Y, Lan J, Xu Y et al (2024) Ultrafine PtCo alloy by pyrolysis etching-confined pyrolysis for enhanced hydrogen evolution. J Colloid Interface Sci 660:997–1009. https://doi.org/10.1016/j.jcis.2024.01.124

28. Zhou N, Wang R, Liu K (2024) Integrating PtCo nanoparticles on N, S doped pore carbon nanosheets as high-performance bifunctional catalysts for oxygen reduction and hydrogen evolution reactions. J Colloid Interface Sci 654:1186–1198. https://doi.org/10.1016/j.jcis.2023.10.143

29. Cheng Q, Yang S, Fu C et al (2022) High-loaded sub-6 Nm Pt1Co1 intermetallic compounds with highly efficient performance expression in PEMFCs. Energy Environ Sci 15:278–286. https://doi.org/10.1039/D1EE02530A

30. Guo F, Macdonald TJ, Sobrido AJ et al (2023) Recent advances in Ultralow-Pt-Loading electrocatalysts for the efficient hydrogen evolution. Adv Sci 10:2301098. https://doi.org/10.1002/advs.202301098

31. Anantharaj S, Noda S (2022) Layered 2D PtX_2 (X=S, Se, Te) for the electrocatalytic HER in comparison with Mo/WX_2 and Pt/C: are we missing the bigger picture? Energy Environ Sci 15:1461–1478. https://doi.org/10.1039/D1EE03516A

32. Zeng Z, Küspert S, Balaghi SE et al (2023) Ultrahigh mass activity Pt entities consisting of Pt single atoms, clusters, and nanoparticles for improved hydrogen evolution reaction. Small 19:2205885. https://doi.org/10.1002/smll.202205885

Authors and Affiliations

Huiyu Li[1] · Bin Zhang[1] · Yiqing Jiang[1] · Yanhui Song[1,2] · Xinliang Feng[3] · Peizhi Liu[1] · Junjie Guo[1]

✉ Peizhi Liu
liupeizhi@tyut.edu.cn

✉ Junjie Guo
guojunjie@tyut.edu.cn

1   Key Laboratory of Interface Science and Engineering in Advanced Materials, Ministry of Education, College of Materials Science and Engineering, Taiyuan University of Technology, Taiyuan 030024, P. R. China

2   Instrumental Analysis Center, Taiyuan University of Technology, Taiyuan 030024, P. R. China

3   Shanxi Qingfeng New Materials Technology CO., LTD, Jinzhong 030606, P. R. China